

A MOF-Based Spatial-Separation Layer to Enable a Uniform Favorable Microenvironment for Electrochemical CO₂ Reduction

Xu Han, Ting Zhang,* Martí Biset-Peiró, Siqi Zhao, Sebastian Murcia Lopez, Kim Daasbjerg, Joan Ramon Morante, Jian Li,* and Jordi Arbiol*

Regulating the local microenvironment of active sites to increase their specific CO₂ concentration and pH gradient, is a promising approach to optimize the electrochemical CO₂ reduction reaction (eCO₂RR). However, currently reported morphological strategies display an uncertainty to the compatibility and distribution between catalytic sites and their microenvironment. Here, a uniform spatial-separation metal–organic framework (MOF) layer between active sites and bulk electrolyte is proposed, which enables each active site to locate in a similarly favorable microenvironment. Zinc oxide (ZnO) nanorods (NR), a representative electrocatalyst for eCO₂RR, is covered with a Zeolitic imidazolate framework-8 (ZIF-8) thin layer to serve as a model system. The prepared ZnO NR@ZIF-8 exhibits an enhanced Faradaic efficiency toward CO at a wide range of potentials and reaches a maximum FE of CO (85%) at –1.05 V versus reversible hydrogen electrode, which is one of the best records till date. Moreover, the hydrophobic ZIF-8 layer protects ZnO against self-reduction. Such performance benefits from the porous ZIF-8 shell with high CO₂ affinity, realizing efficient CO₂ access and retaining an increased local pH near ZnO active sites.

1. Introduction


Electrochemical CO₂ reduction reaction (eCO₂RR) is a promising method to produce value-added chemicals and commodities, which can help to tackle the anthropogenic CO₂ in the atmosphere and achieve a sustainable redox cycle for energy storage and conversion.^[1] Because of the sluggish reaction kinetics of multi-proton and multi-electron transfer in the CO₂ reduction process and the competitive hydrogen evolution reaction (HER) occurring under aqueous conditions, substantial efforts have been invested toward the design of new electrocatalysts with improved activity and selectivity.^[2] In addition to optimization of the intrinsic catalytic activity, the local environment around catalysts, closely related to the transportation of reaction species and intermediates, also plays an important role.^[3] As the

catalytic process has a synergistic effect between the active sites and the corresponding local microenvironment, judiciously integrating the intrinsic activity of catalysts with a favorable local

X. Han, T. Zhang, J. Arbiol
Advanced Electron Nanoscopy
Catalan Institute of Nanoscience and Nanotechnology (ICN2), CSIC and BIST
Campus UAB Bellaterra, 08193 Barcelona, Catalonia, Spain
E-mail: ting.zhang@icn2.cat; arbiol@icrea.cat

X. Han, T. Zhang, M. Biset-Peiró, S. Murcia Lopez, J. R. Morante
Energy Storage, Harvesting and Catalysis Group
Catalonia Institute for Energy Research (IREC)
Sant Adrià de Besòs, 08930 Barcelona, Catalonia, Spain

S. Zhao, K. Daasbjerg
Department of Chemistry/Interdisciplinary Nanoscience Center (iNANO)
Aarhus University
Langelandsgade 140, 8000 Aarhus C, Denmark

 The ORCID identification number(s) for the author(s) of this article can be found under <https://doi.org/10.1002/ssstr.202200388>.

© 2023 The Authors. Small Structures published by Wiley-VCH GmbH. This is an open access article under the terms of the Creative Commons Attribution License, which permits use, distribution and reproduction in any medium, provided the original work is properly cited.

DOI: 10.1002/ssstr.202200388

S. Zhao, K. Daasbjerg
Novo Nordisk Foundation (NNF) CO₂ Research Center (CORC)
Aarhus University
Gustav Wieds Vej 10C, 8000 Aarhus C, Denmark

J. R. Morante
Department of Physics
Universitat de Barcelona
08028 Barcelona, Catalonia, Spain

J. Li
Laboratory of Renewable Energy Science and Engineering
Institute of Mechanical Engineering
EPFL
Station 9, 1015 Lausanne, Switzerland
E-mail: jian.li@epfl.ch

J. Arbiol
ICREA
Pg. Lluís Companys 23, 08010 Barcelona, Catalonia, Spain

environment is a wise strategy to achieve efficient catalytic performance.^[4]

The accessibility to high concentrations of CO₂ and the retainability of increased local pH near the catalysts are two crucial parameters for the optimization of the local microenvironment.^[5] Under high local CO₂ concentration and elevated pH, the active sites will promote the reduction of CO₂ and inhibit HER.^[6] For example, E. H. Sargent's group prepared nanoneedle-like Au tips to achieve an enhanced local concentration of CO₂ around the nanometer-sized tips of the needle via field-induced reagent concentration.^[7] In contrast, Y. Surendranath and coworkers reported that ordered mesostructured electrodes elevated the local pH to promote CO₂-to-CO transformation.^[8] Recently, Züttel's group reported that a highly porous electrocatalyst structure could strengthen the local pH effect, thus promoting CO selectivity by suppressing HER.^[9] However, the aforementioned morphological strategies, which construct a favorable microenvironment via regulating the morphology of catalysts, bring more uncertainty to the compatibility and distribution between catalytic sites and microenvironment during the optimization process. To eliminate this inconsistency between catalytic sites and the local environment, it is reasonable to utilize a spatial separation strategy to construct a uniform and well-defined interface layer. In this scenario,

all the active sites would be placed under a similarly favorable microenvironment, which would not only simplify their characterization and optimization, but also maximize the synergy between them and their local microenvironment.

To build a uniform spatial-separation microenvironment for each active site, introducing functional material with CO₂ enrichment effect and ordered porous structure between the active sites and the bulk electrolyte is an appealing approach. Zeolitic imidazolate framework-8 (ZIF-8) possesses large specific surface area, permanent porosity, and excellent CO₂ enrichment capacity, making it of great potential to construct such a favorable spatial-separation interface.^[10] As a proof of concept, zinc oxide (ZnO) nanorods (NR), a representative electrocatalyst for eCO₂RR,^[11] were coated with a ZIF-8 thin sheath to serve as a model system. To avoid residual surfactants on the ZnO surface, the growth of ZIF-8 layer was achieved via an inorganic template-assisted method. Compared to the pristine ZnO, the ZnO NR@ZIF-8 exhibited much higher activity and selectivity toward CO at a wide range of potentials and reached a maximum Faradaic efficiency of CO (FE_{CO}) of 85% at -1.05 V versus reversible hydrogen electrode (RHE). This latest FE_{CO} value for ZnO NR@ZIF-8 is one of the best values for ZnO-based catalysts reported till date. Moreover, the ZIF-8 thin layer kept the whole

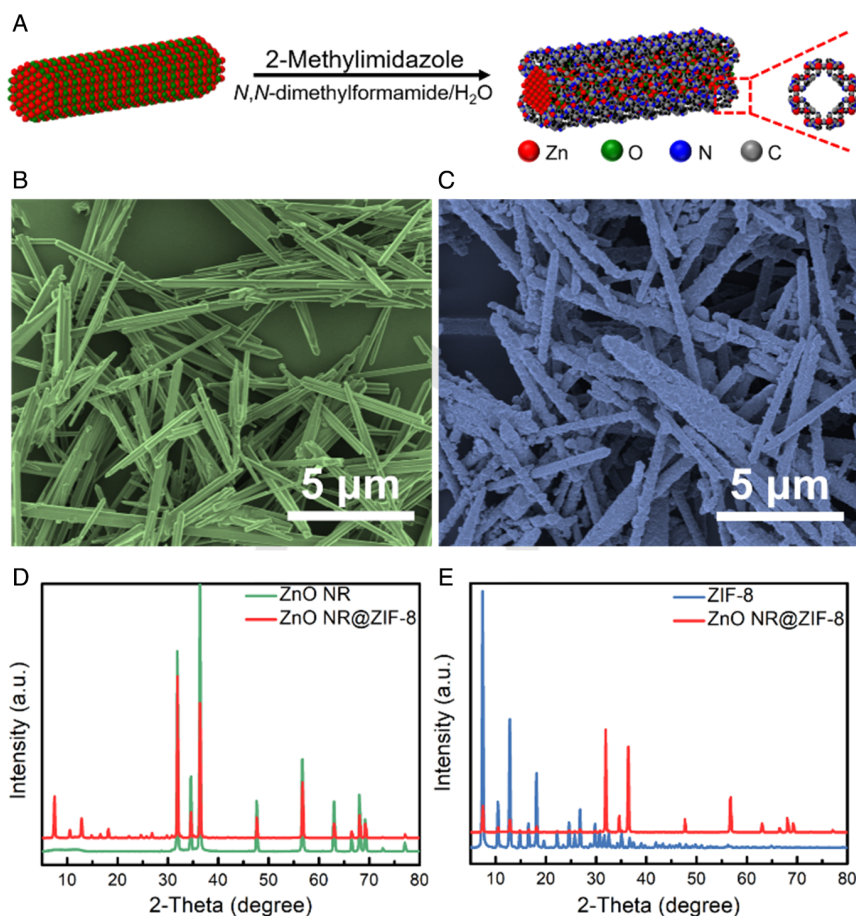


Figure 1. A) Schematic illustration of the formation process of ZnO NR@zeolitic imidazolate framework (ZIF-8) with scanning electron microscope (SEM) images of B) ZnO NR and C) ZnO NR@ZIF-8. X-ray diffraction (XRD) patterns of D) ZnO NR and ZnO NR@ZIF-8 and E) ZIF-8, and ZnO NR@ZIF-8.

structure more stable during eCO₂RR. Buffer electrolytes and wet-ability experiments proved that such enhancement was attributed to the increased pH and local CO₂ concentration, resulting from the uniform spatial-separation interface. These results demonstrate the excellence of constructing a uniform spatial-separation interface layer to achieve the integration of active sites with a favorable local microenvironment, which provides valuable insights for the rational design of future high-efficient electrocatalysts.

2. Results and Discussion

ZnO NR@ZIF-8 was prepared by an inorganic template-assisted synthesis procedure (Figure 1A).^[12] In brief, ZnO NR were first prepared and then used as self-sacrificed templates for subsequent in situ growth of ZIF-8 in *N,N*-dimethylformamide (DMF) solution of 2-methylimidazole without any additional surfactant. Field-emission scanning electron microscopy (FE-SEM) was used to characterize the morphology of the prepared ZnO NR@ZIF-8, ZnO, and ZIF-8 samples. In comparison to the pristine ZnO NR sample (Figure S1, Supporting Information) and pure ZIF-8 (Figure S2, Supporting Information), it was clearly observed that the ZnO NR@ZIF-8 inherited a rodlike structure from ZnO NR with an additional rough surface (Figure 1B,C). The crystallinity of the as-prepared samples was confirmed by powder X-ray diffraction (XRD) measurements. Due to the different feature peaks, the XRD pattern for ZnO NR@ZIF-8 exhibited two kinds of distinct crystal structures. Except for the diffraction peaks after 30° corresponding to the XRD pattern of ZnO NR, the

new diffraction peaks before 20° were assigned to ZIF-8 (Figures 1D,E and S3, Supporting Information).^[11a,11b,13] To further prove the uniform distribution of the ZIF-8 shell on the ZnO NR, transmission electron microscopy (TEM) characterization was carried out. Thanks to the difference of contrast in bright-field (BF) TEM and the high-angle annular dark-field scanning TEM (HAADF-STEM) images (Figure 2A–C), we could observe that the entire surface of ZnO NR was covered with a uniform shell, demonstrating that ZIF-8 was uniformly grown on the ZnO NRs surface. Elemental composition maps were further obtained by means of electron energy loss spectroscopy (EELS) in STEM mode (Figure 2D). N and C elements were mostly located at the outer layer of the nanorod, while Zn was distributed in the whole sample with relatively higher concentration at the core area. It should be noted that N and C elements were only found in the ZIF-8 shell, as part of the ligand, in line with the EELS mapping obtained on the ZIF-8 and ZnO NRs. Based on Fourier-transform infrared spectra, the typical vibration modes expected for ZIF-8 crystals appeared in the ZnO NR@ZIF-8 sample (Figure S4, Supporting Information). N₂ adsorption–desorption measurements were performed to investigate the surface area influenced by the ZIF-8 layer on the as-prepared samples (Figure S5, Supporting Information). The ZnO NR@ZIF-8 catalyst showed a typical type I adsorption/desorption isotherm curve and possessed a high specific surface, indicating that ZnO NR@ZIF-8 had numerous micropores inherited from the ZIF-8 shell. The high volume micropores of ZIF-8 shell could not only improve CO₂ affinities to enhance CO₂ concentration but also provide favorable channels for mass transfer between the active sites

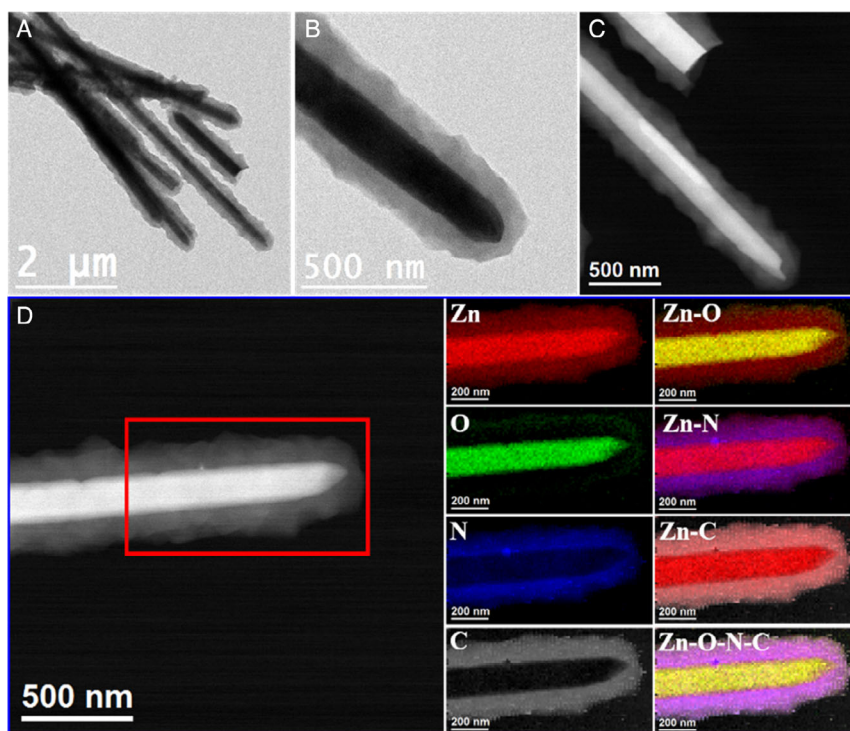


Figure 2. A,B) Bright-field transmission electron microscope (BF TEM) images, C,D) high-angle annular dark-field scanning TEM (HAADF-STEM) images, and representative electron energy loss spectroscopy (EELS) mappings of ZnO NR@ZIF-8.

and the bulk electrolyte.^[14] Additionally, the ZIF-8 layer could control the hydrophobicity of the interface. ZnO NR@ZIF-8 with a water contact angle (CA) of 140° showed a more hydrophobic behavior than that of pure ZnO (water CA of 100°) (Figure S6, Supporting Information), which would inhibit HER and promote the enrichment of CO₂. These results demonstrated that ZnO NRs were uniformly covered by porous ZIF-8 layer, which would create a favorable microenvironment for each active site during eCO₂RR.

The electrocatalytic activity of the different samples toward eCO₂RR was investigated in a typical three-electrode H-cell under CO₂-saturated 0.5 M NaHCO₃ solution. Before the electrochemical measurements, all electrodes were pretreated to obtain a steady current at a constant potential of -0.70 V versus RHE for 30 min (Figure S7A, Supporting Information). Next, linear sweep

voltammetry (LSV) was tested to roughly evaluate the eCO₂RR performance. Notably, ZnO NR@ZIF-8 presented a larger absolute current density in CO₂-saturated electrolyte (Figure S7B, Supporting Information) compared with that in Ar-saturated electrolyte. The absolute total current density of ZnO NR@ZIF-8 and ZnO NR increased significantly with respect to that of ZIF-8 at a wide range of applied potentials, indicating the deterministic role of ZnO as active sites for eCO₂RR (Figure 3A). The fact that the absolute total current density of ZnO NR @ZIF-8 was slightly smaller than that of ZnO demonstrated that core-shell structure did not introduce additional active sites.

As expected, the ZnO NR@ZIF-8 exhibited much higher FE_{CO} than other samples at a cathode potential from -1.15 to -0.80 V versus RHE (Figure 3B). At -1.05 V versus RHE, FE_{CO} of ZnO NR@ZIF-8 was up to 85%, which is one of the

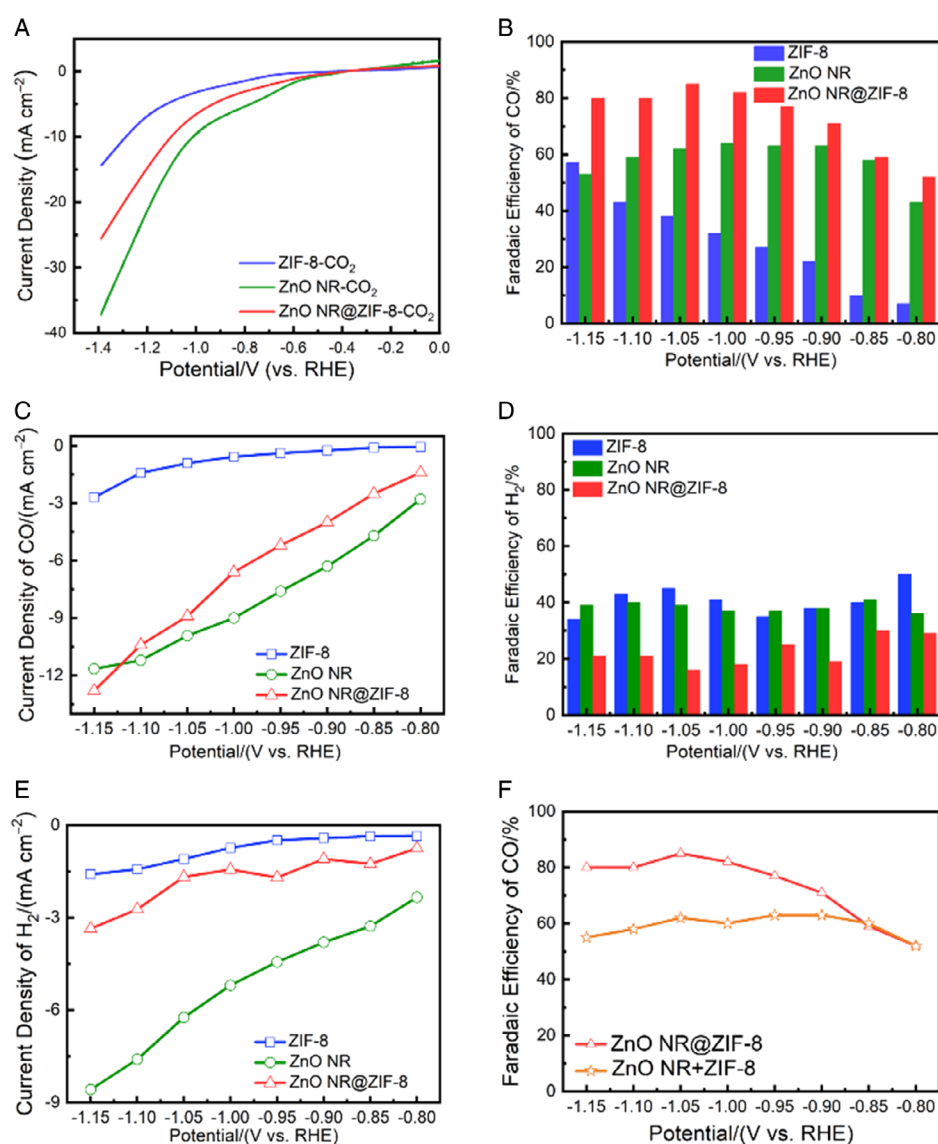


Figure 3. A) Linear sweep voltammetry (LSV) curves acquired in CO₂-saturated 0.5 M NaHCO₃ electrolyte; B) FE of CO at various potentials; C) current density for CO production; D) FE of H₂ at various potentials; E) current density for H₂ production on ZIF-8, ZnO NR, and ZnO NR@ZIF-8; and F) FE of CO at various potentials on the mixture of ZnO NR and ZIF-8, and ZnO NR@ZIF-8 electrodes.

best performances of ZnO-based catalysts (Table S1, Supporting Information). Figure 3C shows the potential-dependent CO partial current densities calculated based on the current densities and corresponding FE_{CO} . Considering the slightly smaller total current density in absolute numbers, the higher CO partial current density of ZnO NR@ZIF-8 was attributed to the presence of the porous ZIF-8 layer, which enabled to provide a favorable microenvironment for ZnO active sites toward CO_2 reduction. For the main side reaction HER, the decreased FE of H_2 was observed when ZIF-8 shell was coated on the surface of ZnO (Figure 3D). The smaller absolute partial H_2 current densities for ZnO NR@ZIF-8 further supported the suppression of HER due to the hydrophobic ZIF-8 layer (Figure 3E). To exclude that such enhancement was attributed to the physical superposition of ZnO NR and ZIF-8, the electrocatalytic activity of a physical mixture of ZnO NR and ZIF-8 was also investigated. Obviously, ZnO NR@ZIF-8 showed a higher FE_{CO} at a wide range of applied potentials than that obtained by the physical mixture of ZnO NRs and ZIF-8 nanostructures (ZnO NR + ZIF-8 sample) (Figure 3F), which indicated that the construction of a spatial-separation interface layer played a crucial role.

To explore the relationship between the shell growth process and the corresponding catalytic activity, a series of core-shell structures were prepared under different solvent composition conditions. A trade-off between the ZnO NR core and ZIF-8 shell was observed during the construction of the spatial-separation interface layer. When DMF was solely used as solvent (sample denoted as 1:0), only small proportion of ZnO NR was covered by the ZIF-8 shell, which could not build an intact interface (Figure S8, Supporting Information). In the case of the ZnO

NR dissolved totally in H_2O (sample denoted as 0:1), no ZIF-8 shell structure was formed, as shown in the corresponding XRD patterns (Figure S9, Supporting Information). With the increase of H_2O in DMF at a certain ratio (i.e., DMF/ H_2O = 7:1, 2:1, 1:1), ZIF-8 could grow on the surface of ZnO NRs, showing a well-defined interface between ZnO and ZIF-8. However, further increasing the ratio of H_2O to DMF/ H_2O = 1:2, the skeleton structure of the NR disappeared (Figure S10, Supporting Information). The CO selectivity (Figure S11, Supporting Information) obtained on different samples demonstrated that the optimal ratio between DMF and H_2O was 7:1. Furthermore, the high local pH around the active sites also benefits the catalytic activity for eCO_2RR and suppressed the HER.^[5c,9] To verify the strengthened local pH effect enabled by ZIF-8 layer, the eCO_2RR of ZnO NR and ZnO NR@ZIF-8 samples were performed in 0.5 M Na_2HPO_4 and 0.5 M $NaHCO_3$, respectively. These two kinds of electrolytes had different buffer capacities (0.5 M Na_2HPO_4 > 0.5 M $NaHCO_3$). Compared to the performance in 0.5 M $NaHCO_3$, the obtained FE_{CO} of ZnO NR was significantly reduced (Figure 4A) while the FE for H_2 was enhanced (Figure 4B) in 0.5 M Na_2HPO_4 . In contrast, ZnO NR@ZIF-8 showed an almost equal FE for CO and H_2 in both electrolytes (Figure 4C,D). Therefore, the nanoporous structure of ZIF-8, to a certain degree, could hinder the neutralization process for OH^- generated from cathodic reactions to keep a higher local pH than that in bulk electrolyte pH, thus suppressing the H_2 evolution and promoting eCO_2RR .

To evaluate the stability of the ZnO NR@ZIF-8 electrocatalyst, we performed a 10 h durability test at a constant potential of

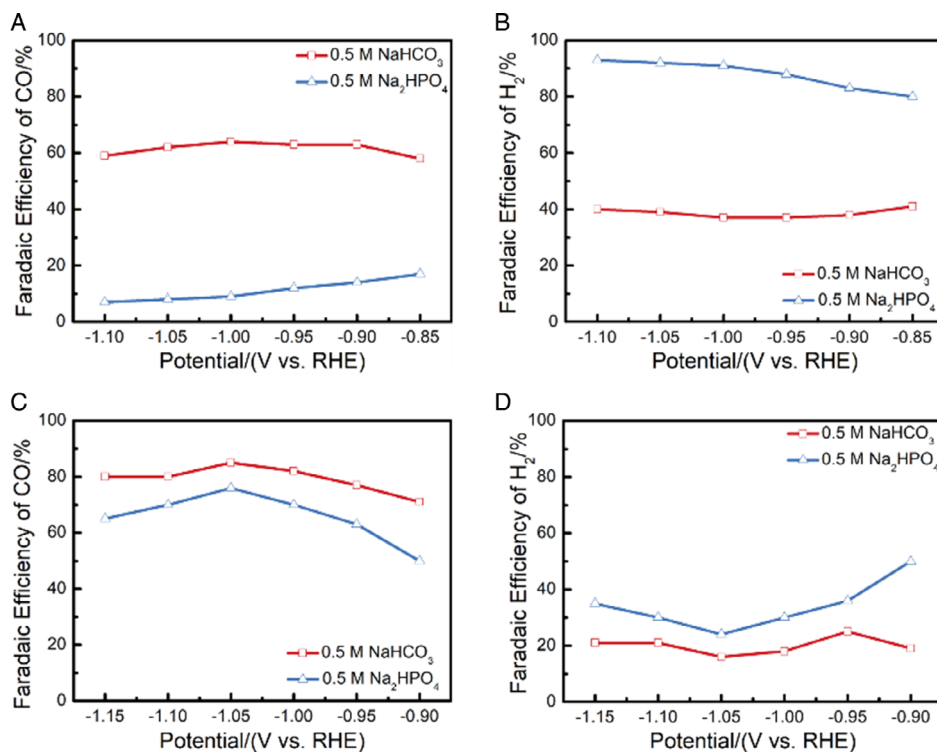


Figure 4. A,B) Faradaic efficiency for CO and H_2 on ZnO NR and C,D) ZnO NR@ZIF-8 at various potentials in 0.5 M $NaHCO_3$ and 0.5 M Na_2HPO_4 , respectively.

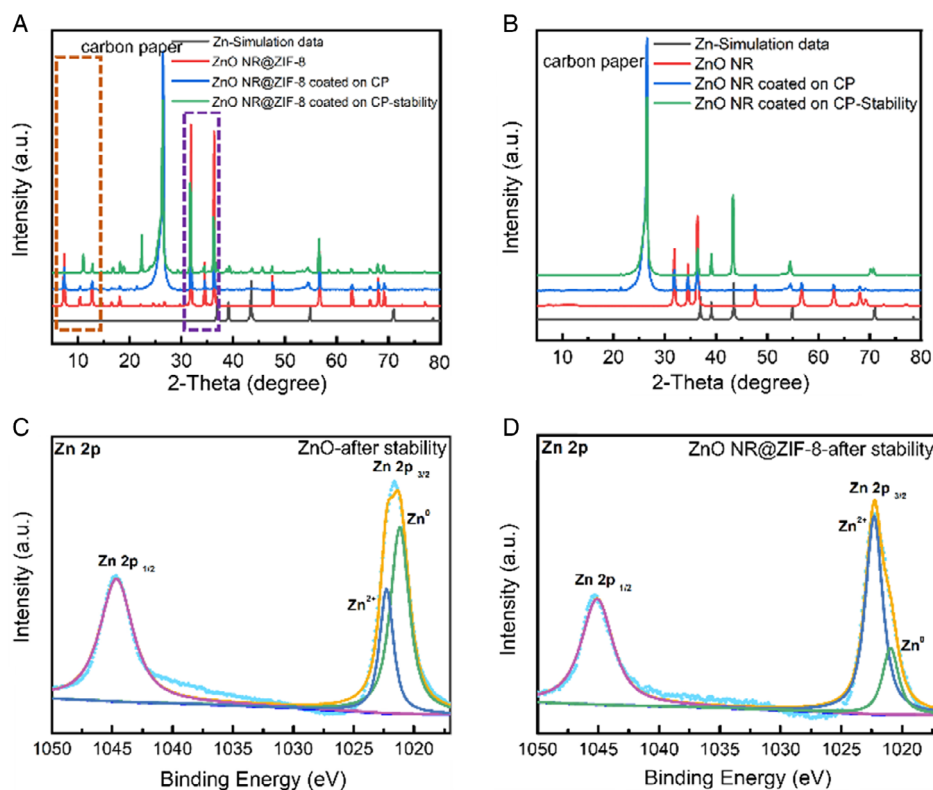


Figure 5. XRD patterns of A) ZnO NR@ZIF-8 and B) ZnO NR after stability test. High-resolution X-ray photoelectron spectroscopy (XPS) Zn 2p spectra of C) ZnO NR and D) ZnO NR@ZIF-8 after stability test.

–1.05 V versus RHE. The outlet gas was analyzed every 30 min by gas chromatography, while calculating the corresponding FE of CO. The current density of ZnO NR@ZIF-8 maintained a steady value of approximately -13 mA cm^{-2} with no significant decay (Figure S12, Supporting Information), and the corresponding FE of CO remained $>80\%$ during the 10 h test. As a comparison, the stability of bare ZnO NR was also performed. Interestingly, the color of bare ZnO NR electrode turned black from white, which was ascribed to the reduction of ZnO to Zn.^[11a,15] In contrast, the color of ZnO NR@ZIF-8 electrode kept unchanged, indicating that the higher local concentration of CO₂ near ZnO active sites could promote eCO₂RR while inhibiting its self-reduction (Figure S13, Supporting Information).

XRD, X-ray photoelectron spectroscopy (XPS), and TEM were used to obtain more accurate analysis of the structure and composition of the electrocatalysts after the stability test. Unlike the ZnO NR@ZIF-8, which only displayed the characteristic peaks of ZnO and ZIF-8 (Figure 5A), the XRD spectra obtained on the ZnO NR after stability showed new emerging characteristic peaks belonging to metallic Zn (Figure 5B). Similarly, compared to the XPS spectra obtained on ZnO NR@ZIF-8 after stability, the XPS spectra obtained on the ZnO NR presented a much stronger peak ascribed to the zero-valent zinc, in line with the XRD results (Figure 5C,D). The morphology of ZnO NR@ZIF-8 did not change after the stability test, according to the results obtained by TEM and HAADF-STEM images. In addition, the EELS compositional maps showed that the ZIF-8 shell was still homogeneously covering the ZnO NR surface

and the interface between them was still clearly observed (Figure S14, Supporting Information). All these results clearly demonstrated that the ZIF-8 interface layer facilitated the ZnO active sites to participate in eCO₂RR efficiently, thus stabilizing ZnO against reduction.

3. Conclusion

In summary, a ZIF-8 shell has been introduced on the surface of ZnO NRs by an in situ growth method, which provides a uniformly favorable microenvironment for eCO₂RR. Compared to pristine ZnO, the ZnO NR@ZIF-8 realizes a much higher FE_{CO} with a maximum of 85% at –1.05 V versus RHE. Moreover, the ZIF-8 thin layer protects the ZnO NR and keeps them stable during the eCO₂RR. Such performance is attributed to the following aspects: 1) the hydrophobic ZIF-8 shell layer enables a higher CO₂ concentration around the active sites and alleviates the water penetration to ZnO surface; and 2) the highly porous structure of ZIF-8 strengthens the local pH near ZnO, which further promotes the catalytic selectivity of eCO₂RR via suppressing HER. This work provides a spatial-separation strategy to create a uniformly favorable local microenvironment for each active site, paving a new way for the improvement of eCO₂RR.

Supporting Information

Supporting Information is available from the Wiley Online Library or from the author.

Acknowledgements

The authors acknowledge funding from Generalitat de Catalunya 2021 SGR 01581 and 2021 SGR 00457. X.H., T.Z., M.B.-P., S.M.L., J.R.M., and J.A. acknowledge funding from the projects (Grant nos. PID2020-116093RB-C42 and -C43), funded by MCIN/AEI/10.13039/501100011033/and by “ERDF A way of making Europe”, by the “European Union”. This study was supported by MCIN with funding from European Union NextGenerationEU (PRTR-C17.11) and Generalitat de Catalunya. ICN2 is supported by the Severo Ochoa program from Spanish MCIN/AEI (Grant no. CEX2021-001214-S). S.Z. and K.D. acknowledge Novo Nordisk Foundation CO₂ Research Center (Grant no. NNF21SA0072700). ICN2 and IREC are funded by the CERCA Programme/Generalitat de Catalunya. Part of the present work has been performed in the framework of Universitat Autònoma de Barcelona Materials Science PhD program. X.H. thanks China Scholarship Council for scholarship support (Grant no. 201804910551).

Conflict of Interest

The authors declare no conflict of interest.

Data Availability Statement

The data that support the findings of this study are available from the corresponding author upon reasonable request.

Keywords

CO generation, CO₂, electrocatalyses, microenvironments, spatial-separation layers

Received: December 13, 2022

Revised: February 20, 2023

Published online: March 9, 2023

- [1] a) F. Pan, Y. Yang, *Energy Environ. Sci.* **2020**, *13*, 2275; b) J. Qiao, Y. Liu, F. Hong, J. Zhang, *Chem. Soc. Rev.* **2014**, *43*, 631; c) S.-J. Shin, H. Choi, S. Ringe, D. H. Won, H.-S. Oh, D. H. Kim, T. Lee, D.-H. Nam, H. Kim, C. H. Choi, *Nat. Commun.* **2022**, *13*, 5482; d) Q. Wang, K. Liu, J. Fu, C. Cai, H. Li, Y. Long, S. Chen, B. Liu, H. Li, W. Li, X. Qiu, N. Zhang, J. Hu, H. Pan, M. Liu, *Angew. Chem. Int. Ed.* **2021**, *60*, 25241; e) Q. Wang, K. Liu, J. Fu, C. Cai, H. Li, Y. Long, S. Chen, B. Liu, H. Li, W. Li, X. Qiu, N. Zhang, J. Hu, H. Pan, M. Liu, *Angew. Chem.* **2021**, *133*, 25445; f) Z.-K. Xin, M.-Y. Huang, Y. Wang, Y.-J. Gao, Q. Guo, X.-B. Li, C.-H. Tung, L.-Z. Wu, *Angew. Chem. Int. Ed.* **2022**, *61*, e202207222; g) Z.-K. Xin, M.-Y. Huang, Y. Wang, Y.-J. Gao, Q. Guo, X.-B. Li, C.-H. Tung, L.-Z. Wu, *Angew. Chem.* **2022**, *134*, e202207222.
- [2] a) T. Zhang, X. Han, H. Liu, M. Biset-Peiró, X. Zhang, P. Tan, P. Tang, B. Yang, L. Zheng, J. R. Morante, J. Arbiol, *Energy Environ. Sci.* **2021**, *14*, 4847; b) T. Zhang, X. Han, H. Liu, M. Biset-Peiró, J. Li, X. Zhang, P. Tang, B. Yang, L. Zheng, J. R. Morante, J. Arbiol, *Adv. Funct. Mater.* **2022**, *32*, 2111446; c) S. Lin, C. S. Diercks, Y.-B. Zhang, N. Kornienko, E. M. Nichols, Y. Zhao, A. R. Paris, D. Kim, P. Yang, O. M. Yaghi, C. J. Chang, *Science* **2015**, *349*, 1208; d) G. Wang, J. Chen, Y. Ding, P. Cai, L. Yi, Y. Li, C. Tu, Y. Hou, Z. Wen, L. Dai, *Chem. Soc. Rev.* **2021**, *50*, 4993; e) Q. Guo, F. Liang, X.-B. Li, Y.-J. Gao, M.-Y. Huang, Y. Wang, S.-G. Xia, X.-Y. Gao, Q.-C. Gan, Z.-S. Lin, C.-H. Tung, L.-Z. Wu, *Chem* **2019**, *5*, 2605; f) J. Li, X. Gao, L. Zhu, M. N. Ghazzal, J. Zhang, C.-H. Tung, L.-Z. Wu, *Energy Environ. Sci.* **2020**, *13*, 1326.
- [3] a) J.-J. Lv, R. Yin, L. Zhou, J. Li, R. Kikas, T. Xu, Z.-J. Wang, H. Jin, X. Wang, S. Wang, *Angew. Chem. Int. Ed.* **2022**, *61*, e202207252; b) J.-J. Lv, R. Yin, L. Zhou, J. Li, R. Kikas, T. Xu, Z.-J. Wang, H. Jin, X. Wang, S. Wang, *Angew. Chem.* **2022**, *134*, e202207252; c) H.-K. Lim, Y. Kwon, H. S. Kim, J. Jeon, Y.-H. Kim, J.-A. Lim, B.-S. Kim, J. Choi, H. Kim, *ACS Catal.* **2018**, *8*, 2420; d) S. E. Weitzner, S. A. Akhade, J. B. Varley, B. C. Wood, M. Otani, S. E. Baker, E. B. Duoss, *J. Phys. Chem. Lett.* **2020**, *11*, 4113.
- [4] a) C.-T. Dinh, F. P. García de Arquer, D. Sinton, E. H. Sargent, *ACS Energy Lett.* **2018**, *3*, 2835; b) J. Li, X. Han, D. Wang, L. Zhu, M.-H. Ha-Thi, T. Pino, J. Arbiol, L.-Z. Wu, M. Nawfal Ghazzal, *Angew. Chem. Int. Ed.* **2022**, *61*, e202210242; c) J. Li, X. Han, D. Wang, L. Zhu, M.-H. Ha-Thi, T. Pino, J. Arbiol, L.-Z. Wu, M. Nawfal Ghazzal, *Angew. Chem.* **2022**, *134*, e202210242.
- [5] a) J. Li, G. Chen, Y. Zhu, Z. Liang, A. Pei, C.-L. Wu, H. Wang, H. R. Lee, K. Liu, S. Chu, Y. Cui, *Nat. Catal.* **2018**, *1*, 592; b) R. Shi, J. Guo, X. Zhang, G. I. N. Waterhouse, Z. Han, Y. Zhao, L. Shang, C. Zhou, L. Jiang, T. Zhang, *Nat. Commun.* **2020**, *11*, 3028; c) M. Ma, B. J. Trzeźniewski, J. Xie, W. A. Smith, *Angew. Chem. Int. Ed.* **2016**, *55*, 9748; d) M. Ma, B. J. Trzeźniewski, J. Xie, W. A. Smith, *Angew. Chem.* **2016**, *128*, 9900; e) W. Ge, Y. Chen, Y. Fan, Y. Zhu, H. Liu, L. Song, Z. Liu, C. Lian, H. Jiang, C. Li, *J. Am. Chem. Soc.* **2022**, *144*, 6613; f) H.-Q. Liang, S. Zhao, X.-M. Hu, M. Ceccato, T. Skrydstrup, K. Daasbjerg, *ACS Catal.* **2021**, *11*, 958; g) B. Yang, K. Liu, H. Li, C. Liu, J. Fu, H. Li, J. E. Huang, P. Ou, T. Alkayyali, C. Cai, Y. Duan, H. Liu, P. An, N. Zhang, W. Li, X. Qiu, C. Jia, J. Hu, L. Chai, Z. Lin, Y. Gao, M. Miyauchi, E. Cortés, S. A. Maier, M. Liu, *J. Am. Chem. Soc.* **2022**, *144*, 3039; h) H. Li, H. Zhou, Y. Zhou, J. Hu, M. Miyauchi, J. Fu, M. Liu, *Chin. J. Catal.* **2022**, *43*, 519–525.
- [6] a) K. Yang, R. Kas, W. A. Smith, *J. Am. Chem. Soc.* **2019**, *141*, 15891; b) S. Mu, L. Li, R. Zhao, H. Lu, H. Dong, C. Cui, *ACS Appl. Mater. Interfaces* **2021**, *13*, 47619.
- [7] a) M. Liu, Y. Pang, B. Zhang, P. De Luna, O. Voznyy, J. Xu, X. Zheng, C. T. Dinh, F. Fan, C. Cao, F. P. G. de Arquer, T. S. Safaei, A. Mepham, A. Klinkova, E. Kumacheva, T. Filleter, D. Sinton, S. O. Kelley, E. H. Sargent, *Nature* **2016**, *537*, 382; b) T. Saberi Safaei, A. Mepham, X. Zheng, Y. Pang, C.-T. Dinh, M. Liu, D. Sinton, S. O. Kelley, E. H. Sargent, *Nano Lett.* **2016**, *16*, 7224.
- [8] a) Y. Yoon, A. S. Hall, Y. Surendranath, *Angew. Chem. Int. Ed.* **2016**, *55*, 15282; b) A. S. Hall, Y. Yoon, A. Wuttig, Y. Surendranath, *J. Am. Chem. Soc.* **2015**, *137*, 14834.
- [9] W. Luo, J. Zhang, M. Li, A. Züttel, *ACS Catal.* **2019**, *9*, 3783.
- [10] a) Y. Li, K. Wang, W. Zhou, Y. Li, R. Vila, W. Huang, H. Wang, G. Chen, G.-H. Wu, Y. Tsao, H. Wang, R. Sinclair, W. Chiu, Y. Cui, *Matter* **2019**, *1*, 428; b) K. S. Park, Z. Ni, A. P. Côté, J. Y. Choi, R. Huang, F. J. Uribe-Romo, H. K. Chae, M. O’Keeffe, O. M. Yaghi, *Proc. Natl. Acad. Sci.* **2006**, *103*, 10186; c) H. Luo, B. Li, J.-G. Ma, P. Cheng, *Angew. Chem. Int. Ed.* **2022**, *61*, e202116736; d) H. Luo, B. Li, J.-G. Ma, P. Cheng, *Angew. Chem.* **2022**, *134*, e202116736.
- [11] a) X. Han, T. Zhang, M. Biset-Peiró, X. Zhang, J. Li, W. Tang, P. Tang, J. R. Morante, J. Arbiol, *ACS Appl. Mater. Interfaces* **2022**, *14*, 32157; b) Z. Geng, X. Kong, W. Chen, H. Su, Y. Liu, F. Cai, G. Wang, J. Zeng, *Angew. Chem. Int. Ed.* **2018**, *57*, 6054; c) Z. Geng, X. Kong, W. Chen, H. Su, Y. Liu, F. Cai, G. Wang, J. Zeng, *Angew. Chem.* **2018**, *130*, 6162; d) D. L. T. Nguyen, M. S. Jee, D. H. Won, H. Jung, H.-S. Oh, B. K. Min, Y. J. Hwang, *ACS Sustainable Chem. Eng.* **2017**, *5*, 11377; e) Q. Xiang, F. Li, J. Wang, W. Chen, Q. Miao, Q. Zhang, P. Tao, C. Song, W. Shang, H. Zhu, T. Deng, J. Wu, *ACS Appl. Mater. Interfaces* **2021**, *13*, 10837.

- [12] a) W.-W. Zhan, Q. Kuang, J.-Z. Zhou, X.-J. Kong, Z.-X. Xie, L.-S. Zheng, *J. Am. Chem. Soc.* **2013**, *135*, 1926; b) C. Young, J. Wang, J. Kim, Y. Sugahara, J. Henzie, Y. Yamauchi, *Chem. Mater.* **2018**, *30*, 3379; c) S. Dai, A. Tissot, C. Serre, *Adv. Energy Mater.* **2022**, *12*, 2100061.
- [13] a) Q. Shi, Z. Chen, Z. Song, J. Li, J. Dong, *Angew. Chem. Int. Ed.* **2011**, *50*, 672; b) Q. Shi, Z. Chen, Z. Song, J. Li, J. Dong, *Angew. Chem.* **2011**, *123*, 698.
- [14] a) M. B. Gawande, P. Fornasiero, R. Zbořil, *ACS Catal.* **2020**, *10*, 2231; b) Q. Lu, C. Chen, Q. Di, W. Liu, X. Sun, Y. Tuo, Y. Zhou, Y. Pan, X. Feng, L. Li, D. Chen, J. Zhang, *ACS Catal.* **2022**, *12*, 1364.
- [15] a) W. Deng, L. Zhang, L. Li, S. Chen, C. Hu, Z.-J. Zhao, T. Wang, J. Gong, *J. Am. Chem. Soc.* **2019**, *141*, 2911; b) W. Luo, Q. Zhang, J. Zhang, E. Moiola, K. Zhao, A. Züttel, *Appl. Catal., B* **2020**, *273*, 119060.